Materials Today Energy 40 (2024) 101488

Contents lists available at ScienceDirect

Materials Today Energy

journal homepage: www.journals.elsevier.com/materials-today-energy/

# Separator pore size induced oriented Zn deposition

Kesong Yu [a], Yuehua Wen [a], Mengyu Yan [a, d, *], Xuan Teng [a], Wei Yang [a], Sitian Lian [a], Jianyong Zhang [a], Farao Zhang [b], Xiaoyu Jiang [b, **], Yanzhu Luo [c, ***], Liqiang Mai [a, d, ****]

[a] State Key Laboratory of Advanced Technology for Materials Synthesis and Processing, School of Materials Science and Engineering, International School of Materials Science and Engineering, Wuhan University of Technology, Wuhan, 430070, China
[b] Ningbo MaterChem Technology Co. Ltd, Ningbo, 315830, China
[c] College of Chemistry, Huazhong Agricultural University, Wuhan, 430070, China
[d] Hubei Longzhong Laboratory, Wuhan University of Technology (Xiangyang Demonstration Zone), Xiangyang, 441000, China

ARTICLE INFO

*Article history:*
Received 1 November 2023
Received in revised form
28 December 2023
Accepted 29 December 2023
Available online 2 January 2024

*Keywords:*
Thin separators
*In-situ* XRD
Orientated metal deposition
Zinc batteries

ABSTRACT

Aqueous zinc batteries are promising alternatives to lead-acid batteries for large-scale energy storage. In this work, we developed a $TiO_2$-grafted polyethylene ($TiO_2$-PE) separator for aqueous zinc batteries with excellent hydrophilicity. The $TiO_2$-PE separator demonstrates the thinnest thickness of 9 μm, significantly decreasing the inactive mass of the entire battery comparing with the commercial glass fiber separator. We further prove that the separator pore size can modulate the Zn deposition morphology. The (002)-orientated Zn deposition is induced when the pore size is smaller than the crystal critical length. Therefore, the 0.2 μm pores in $TiO_2$-PE induce a (002)-orientated Zn deposition, while the 2 μm pores in glass fiber lead to a randomly oriented growth of Zn metal. This work highlights the opportunities in the pore size-modulated deposition/stripping process in Zn and other metal batteries.



## 1. Introduction

Aqueous zinc batteries (AZBs) are promising candidates for large-scale energy storage because of their facile fabrication process, environmental friendliness, and intrinsic safety. Additionally, the Zn metal anode offers high theoretical specific capacity (820 mAh/g), low potential (−0.762 V *vs.* standard hydrogen electrode), high abundance, and widespread geological distribution [1–3]. However, the practical application of AZBs is hindered by several challenges. The Zn dendrite grows during plating, for example, due to the inhomogeneous deposition of zinc ions and eventually causes an internal short circuit [4,5].

Recently, various approaches have been developed to address the issues mentioned above, including modifying the Zn anode [6–8], and investigating new electrolytes [9–12]. Despite the separator being an essential component in AZBs, it has received insufficient attention. In most of the literature, glass fiber membranes with a thickness of several hundred micrometers are applied as separators [13,14]. According to Fig. 1 and Table S1 [1,15–20], if the thickness of glass fiber is larger than 400 μm, the energy density of AZBs will be even lower than that of standard lead-acid batteries (30 Wh/kg) [21,22]. Therefore, using glass fiber separators will significantly reduce the overall energy density of AZBs. On the other hand, the glass fiber separator possesses the largest pore sizes 2.7 μm (https://www.whatman.co.kr/pds/03.pdf), which is easy to trigger dendrite formation. The large pores provide sufficient space for dendritic Zn to pass through, causing the degradation of AZBs [13,23].

According to the literature, the crystal critical length of Zn is ~1 μm at 1 mA/cm$^2$ [24,25]. The relatively large pore size of the glass fiber separator allows the deposited Zn crystal to grow into the separator pores. It would be interesting to decrease the pore size to below the Zn crystal critical length, at which the Zn crystals may prefer to grow on the separator surface instead of in the separator pores. Inspired by the investigation of separators in lithium-ion batteries [26–29], a thin polyethylene (PE) membrane is chosen as the substrate of the new AZB separator. Typically, an AZB with a 9-μm PE separator can realize a specific energy of 108 Wh/kg (Fig. 1). More importantly, the small pore size and uniform pore size distribution of the PE separator are beneficial to homogenizing the nucleation and growth of Zn metal [30]. In

* Corresponding author.
** Corresponding author.
*** Corresponding author.
**** Corresponding author.
*E-mail addresses:* ymy@whut.edu.cn (M. Yan), xiaoyuj1991@outlook.com (X. Jiang), luoyanzhu@mail.hzau.edu.cn (Y. Luo), mlq518@whut.edu.cn (L. Mai).

https://doi.org/10.1016/j.mtener.2023.101488
2468-6069/

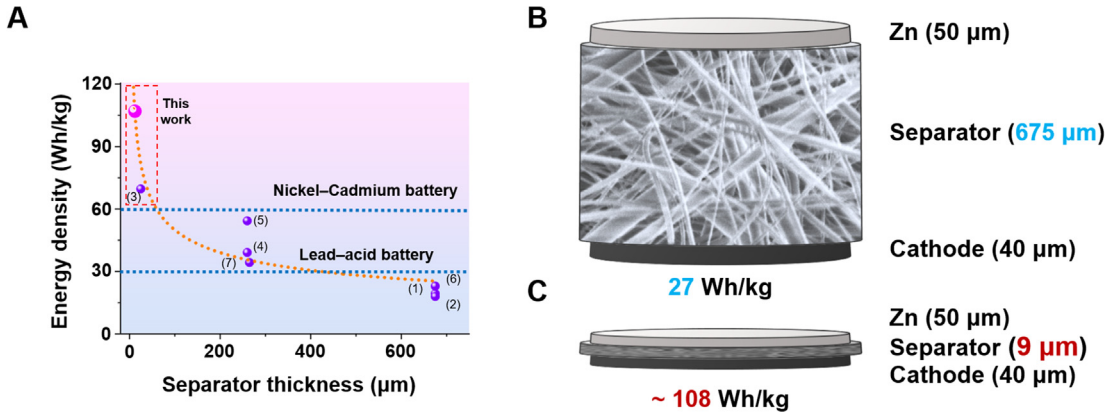


**Fig. 1.** (A) The relationship between separator thickness and energy density of zinc-ion batteries. The energy density is calculated based on the total mass of the cathode, anode, and separator. These separators include commercialized glass fiber, polyethylene, and polypropylene separators [1,15–20]. (B, C) The illustrated configuration of the Zn ion battery with (B) the GF/D glass fiber separator and (C) the thinner polyethylene separators.

addition, utilizing commercial PE separators to construct a durable Zn anode is a facile and low-cost approach highly desirable by the AZBs industry. Herein, we report a simple and scalable approach to prepare a hydrophilic PE separator that is suitable for AZBs (Supporting Information).

## 2. Results and discussion

The $TiO_2$-grafted PE ($TiO_2$-PE) shows obvious hydrophilicity, with a water contact angle of 65.5° (Fig. S1B), much lower than that of pristine PE (123.6°, Fig. S1A). Furthermore, the $TiO_2$-PE separator is immersed in deionized water at room temperature to measure its compatibility with aqueous electrolytes. The $TiO_2$-PE separator becomes transparent and sinks to the bottom of the dish. In contrast, although the plasma-treated PE shows improved water affinity, water cannot penetrate into the inner layer of the PE matrix; it still exhibits the original white color and flows on the water (Fig. S2). Fig. S3A and S3B represent the scanning electron microscopy (SEM) images of the pristine PE and the $TiO_2$-PE separators. The $TiO_2$-PE shows similar surface morphology to the pristine PE, with a highly porous and uniformly interconnected pore structure. This uniform interconnected pore benefits uniform ion transportation and hence flat metal deposition. The pore structure of $TiO_2$-PE is slightly expanded during plasma etching processing, while this effect can be controlled by adjusting the plasma treatment time and power level [31]. Although we have not observed the $TiO_2$ particles on the $TiO_2$-PE separator surface, the Ti $2p_{3/2}$ and $2p_{1/2}$ XPS peaks were found at 458.9 eV and 464.6 eV, indicating Ti was in the +4 valence state (Fig. S4) [32,33]. The further thermal stability test of the $TiO_2$-PE separator confirms the existence of the tiny $TiO_2$ particles (Fig. S5). These tiny particles grafting has a negligible influence on the weight and thickness of the separator, which is suitable for constructing high-energy density AZBs.

The hydrophilicity of the separator is paramount in aqueous zinc ion batteries as it ensures effective electrolyte wetting, facilitates ion transport, reduces internal resistance, and thereby enhances the battery's overall performance. Fig. 2A displays the electrochemical performance of the Zn||Zn symmetric coin cells with 1 M $ZnSO_4$ aqueous electrolyte-filled $TiO_2$-PE, Celgard 3501, or GF/A (glass fiber) separator. The Celgard 3501 is a 25 μm surfactant-coated PP separator and is applicable in aqueous electrolyte battery systems. However, the battery with the Celgard 3501 separator shows a polarization of 109 mV, much larger than that with the $TiO_2$-PE separator (40 mV), indicating that the Celgard 3501 suffers from a low ionic conductivity caused by its inadequate hydrophilicity. The insufficient hydrophilicity of the Celgard 3501 might lead to uneven ion diffusion and evolve into dendrite growth; hence, the battery fails only after 15 h of cycling. The cells with $TiO_2$-PE and GF/A separators exhibit similar polarization at the initial cycles. However, the one with a GF/A separator displays increased polarization, and eventually, an internal short circuit occurs. This result demonstrates that the excellent hydrophilic and uniform pore distribution of the $TiO_2$-PE can ensure the outstanding electrochemical performance of AZBs.

The final morphology of electrodeposited metal critically relies on the initial nucleation behavior. Cyclic voltammetry tests were conducted to explore nucleation behavior, in which Cu foil was used as the cathode, a Zn foil as the anode, and $TiO_2$-PE or GF/A as the separator. As shown in Fig. 2B, the potential located at the A point is called the crossover potential ($E_{co}$). The potential difference between the crossover point (A) and the point (B/B′) where $Zn^{2+}$ start to be reduced on substrates is regarded as the nucleation overpotential (NOP). The NOP is known as a convenient parameter to explain the extent of polarization [34,35]. Here's a formula to describe the relationship between NOP($\eta$) and the critical Zn nucleus radius ($r_{crit}$) [36,37]:

$$r_{crit} = 2\frac{\gamma V_m}{F|\eta|} \quad (1)$$

$\gamma$, $V_m$, and $F$ represent the surface energy at the Zn electrode/electrolyte interface, the molar volume of Zn, and Faraday's constant, respectively. The equation suggests that the higher NOP induces a more fine-grained zinc deposition with favorable crystallographic orientation [38,39]. This increased overpotential provides a sufficient driving force for the nucleation and growth processes with finer nuclei [37,40]. Obviously, the NOP of batteries using the $TiO_2$-PE separator is greater than that of the GF/A separator, which indicates that the former is more conducive to stabilizing the Zn deposition.

To investigate the deposited zinc growth mechanism, we conducted the chronoamperometry test on Zn||Zn symmetric coin cells (Fig. 2C). We could effectively observe nucleation behaviors and surface states by measuring the current variation over time at a constant potential [41–43]. For AZBs with GF/A separator, the current density continued to increase when an overpotential of −150 mV was applied, indicating a long and uncontrolled 3D growth process and rough deposition propagation [44]. The absorbed ions moved laterally along the surface to locate the most favorable energy sites for charge transfer. To minimize surface

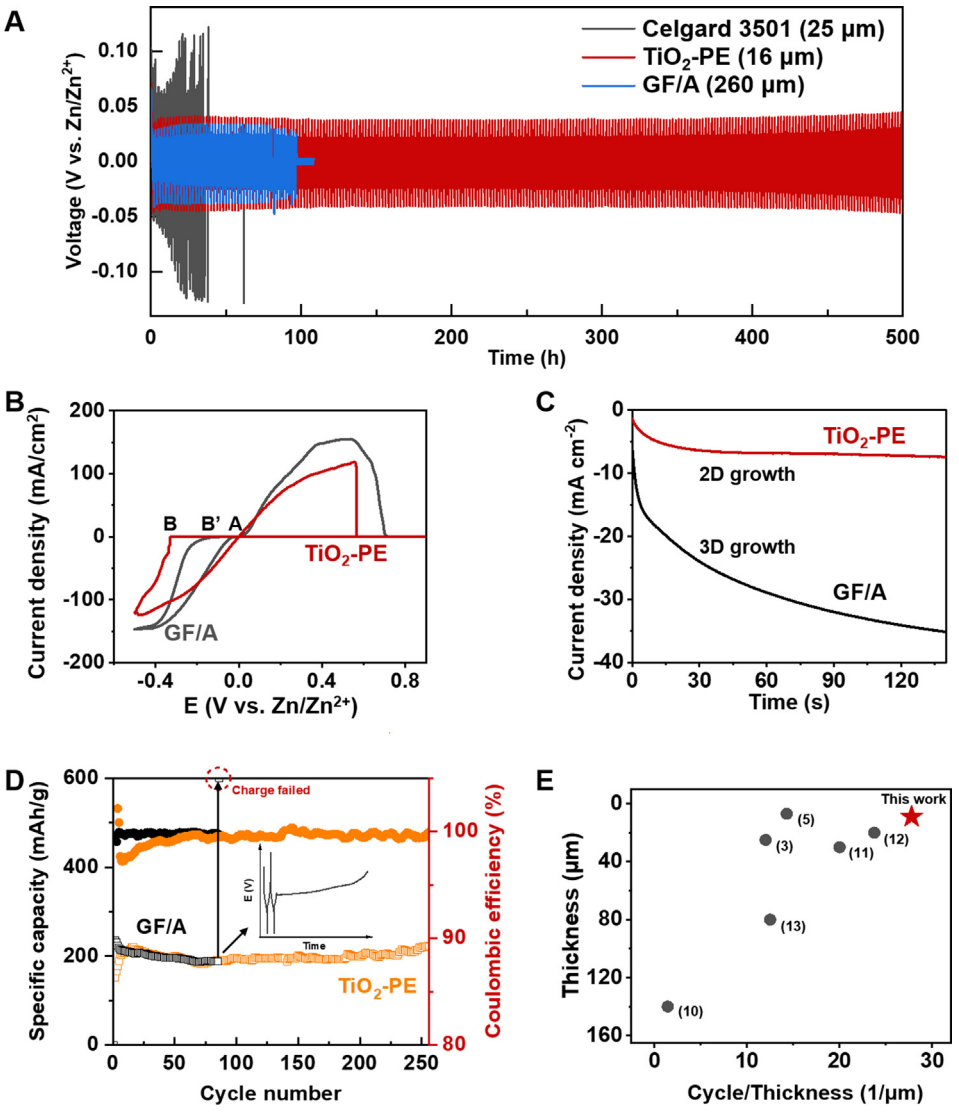


**Fig. 2.** (A) The charge and discharge curves of the Zn||Zn symmetrical batteries with different separators at 1 mA/cm$^2$ and 1 mAh/cm$^2$. (B) Cyclic voltammetry curves for Zn nucleation on the Cu foil with different separators at a scan rate of 0.01 V/s. (C) Chronoamperometry tests with the $TiO_2$-PE and GF/A separators at an overpotential of −150 mV. (D) Cycling performance for the Zn||$VO_2$ full cells with $TiO_2$-PE or GF/A separator at 0.25 A/g. (E) A diagram of the relationship between the cycle number and separators' thickness, reflecting the cycling capability of separators per unit thickness (data from Table S2).

energy and reduce exposed area, $Zn^{2+}$ tended to aggregate and grow into dendrites. In the $TiO_2$-PE separator system, the Zn nucleation and 3D growth processes initially occur for a specific duration. Afterward, a stable and constant 2D growth process continues, suggesting that the $Zn^{2+}$ absorbed on the surface and locally reduced to form zinc metal due to restricted 3D growth [45]. Our findings indicate that the $Zn^{2+}$ tend to deposit very close to the initial absorption site instead of low surface energy tips. These effects lead to an increase in nucleation sites, ultimately promoting the formation of a uniform zinc layer [46,47].

Furthermore, the Zn||$VO_2$ full cells were assembled to explore the practical application of the separators. As shown in Fig. 2D, the Zn||$VO_2$ full cell employing a $TiO_2$-PE separator exhibits remarkable capacity retention of 98 % after 256 cycles at 0.25 A/g, outperforming the Zn||$VO_2$ cell using a GF/A separator, which failed after only 85 cycles. At the same time, $TiO_2$-PE separators can still work at larger current density (Fig. S6). In Fig. 2E and Fig. S7, we show the relationship between cycle per thickness and separator thickness of zinc-ion batteries from the literature, highlighting the advantages of $TiO_2$-PE separators.

The deposition/stripping behavior of zinc metal on this novel separator is studied with *in-situ* X-ray diffraction (XRD). The *in-situ* cell was discharged at a current density of 1 mA/cm$^2$ for 1 h and subsequently charged to an upper cutoff potential of 0.5 V. Fig. 3A and C displays the 'contour-color fill' by combining ~100 XRD patterns. The y-axis represents test time, consistent with the charge/discharge curve, allowing for chasing the crystal structure changes concerning the battery voltage. Fig. 3B and D shows the XRD spectra. In the initial state (Curve A), only the peaks of Be are visible. As the discharge progresses, the intensity of the Zn peaks at 36.1°, 38.8°, 43.1°, and 54.2°, which corresponds to the (002), (100), (101), and (102) crystal planes of Zn [48], respectively, increases significantly and reaches a maximum at the end of the discharge process (Curve B and C). During the charging process, the intensity of the Zn peaks gradually decreases and almost disappears when charged to 0.5 V (Curve D and E), demonstrating a highly reversible

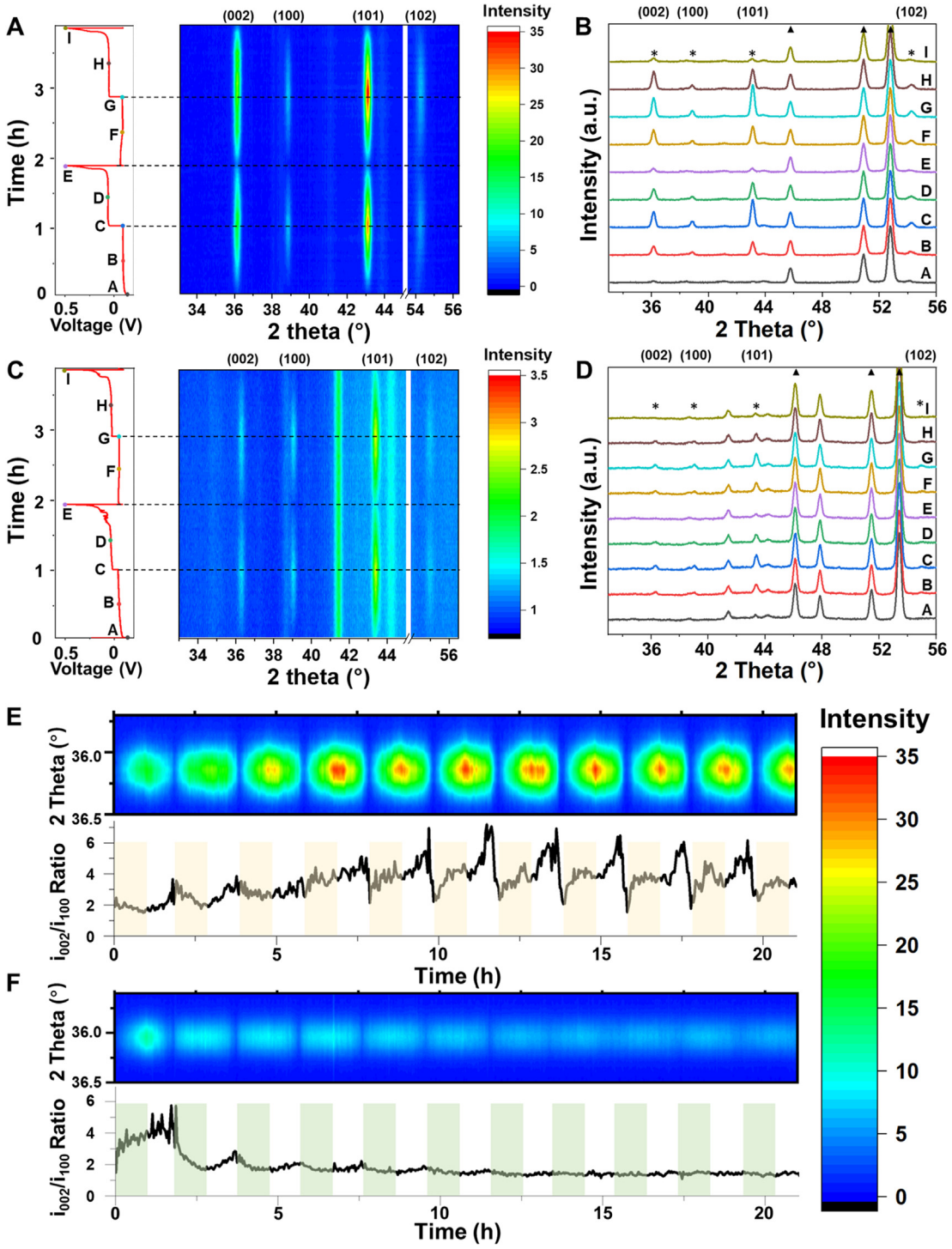


**Fig. 3.** (A–D) *In-situ* XRD patterns of the deposited Zn with the (A and B) $TiO_2$-PE and (C and D) GF/A separator, the symbol ▲ represents the peak of Be while the symbol * represents the peak of Zn; (E and F) The variation of (002) peak intensity and $i_{002}/i_{100}$ ratio of the deposited Zn in the initial 11 cycles with the (E) $TiO_2$-PE and (F) GF/A separators.

Zn plating/stripping performance. The XRD pattern for the battery with a GF/A separator indicates similar variation trends during charging compared to the battery with a $TiO_2$-PE separator, although the peak intensities differ.

Fig. 3E and F shows the *in-situ* XRD pattern of the (002) peak and the $i_{002}/i_{100}$ ratio for the initial 11 cycles with various separators. Recent researches reveal that the (002) plane of the deposited zinc is parallel to the substrate (0–30°), suggesting a smooth and dendrite-free zinc anode [49]. On the contrary, the deposited zinc surface with the (100) plane will present a high angle of 70–90° to the substrate, forming zinc dendrites [50]. For the battery with the $TiO_2$-PE separator, the (002) peak intensity at the discharge endpoint keeps increasing from 17.0 to 33.6 counts in the first four cycles, and then the peak intensity becomes steadied around 32 counts in the following cycles. The $i_{002}/i_{100}$ ratio at the discharge endpoint rises from 2.6 to 6.3 and then levels off, which means that

the proportion of (002) crystal faces reaches a maximum of 86.3 % (Fig. 3E, Fig. S8). For the battery with GF/A, the (002) peak intensity at the discharge endpoint achieves 12.4 counts in the first cycle and then decreases to 6.2 counts after 11 cycles. The $i_{002}/i_{100}$ ratio decreases from 4.0 to 1.3, which means that the proportion of (002) crystal faces is about 56.5 % (Fig. 3F, Fig. S9). This result implies that the Zn crystal orientation along the (002) direction increases during cycling when using the $TiO_2$-PE as the separator.

Morphological analysis of the cycled electrodes was performed using SEM. The results reveal that the Zn crystals on the surface of the $TiO_2$-PE separator exhibit a continuous and flat morphology. However, the Zn crystals on the GF/A surface display varying crystal morphologies, with some growing at a certain inclination and others growing horizontally (Fig. 4E and Fig. S10B). These observations suggest that the growth of Zn crystals is influenced by the surface properties of the electrode material. The SEM images reveal that the Zn crystal is deposited not only on the GF/A separator but also in it. As shown in Fig. 4A and B, pole figures of Zn deposited on $TiO_2$-PE separators represent the lattice-preferred orientation, measured with the electron backscatter diffraction. The SEM results and pole figures suggest that utilizing $TiO_2$-PE as separators enables the preferential growth of (002) planes of Zn during the electrodeposition process, whereas the out-of-plane growth of Zn crystals oriented with the (100) and (101) facets are dominant with the GF/A separator. This conclusion is supported by the electrochemical performance and *in-situ* XRD results with different separators. The superior performance of the $TiO_2$-PE separator is attributed to its small pore size and narrow size distribution (Fig. 4C). During the discharge process, the large pore size of the GF/A separator (Fig. 4D and Fig. S11) allows the Zn crystal to grow between the fibers, resulting in discontinued and inactive Zn. These out-of-plane-grown Zn crystals accumulate during cycling and form dendrites. Since the $TiO_2$-PE pore size (0.21 μm) is one order smaller than the average crystal size of Zn (1.0 μm), the Zn crystals cannot directly

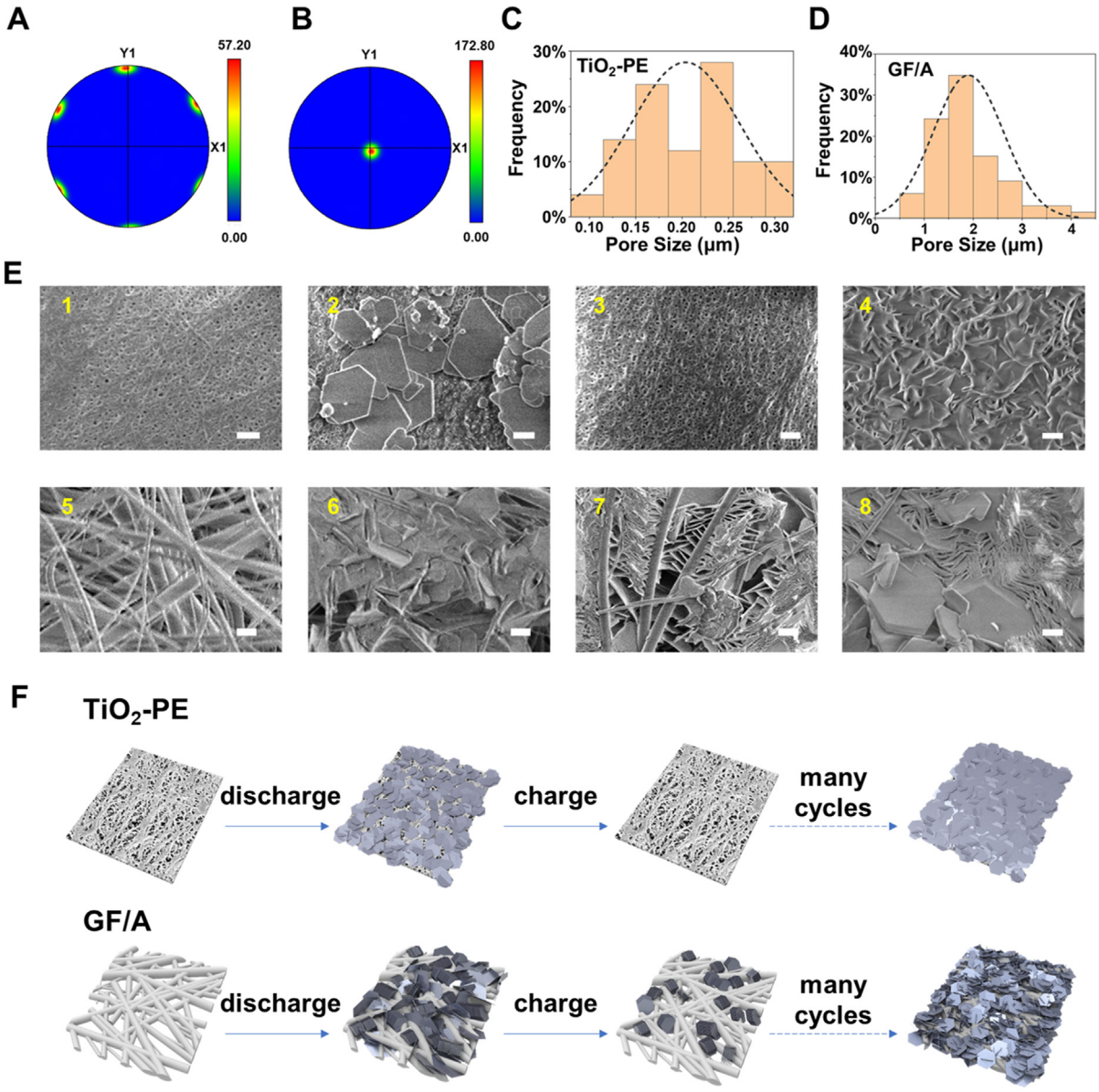


**Fig. 4.** (A–B) (A) {0001} and (B) {11–20} pole figures of deposited Zn on the $TiO_2$-PE separators; (C–D) the pore size distribution of the (C) $TiO_2$-PE and (D) GF/A separators; (E) SEM images of Zn deposition/stripping on $TiO_2$-PE (1–4) and GF/A (5–8) separators (scale bar: 1 μm); (F) Schematic zinc metal deposition/stripping diagram on the $TiO_2$-PE separator and GF/A separator.

grow in the pore structure. Thus, the Zn metal tends to grow horizontally when confined at the $TiO_2$-PE separator and Ti electrode interface (Fig. 4E and F).

## 3. Conclusion

This study presents a facile and industrializable method for manufacturing an ultrathin $TiO_2$-grafted PE separator for aqueous Zinc batteries. The battery with $TiO_2$-PE separator shows excellent electrochemical performance compared with commercial PP or glassy fiber separators. We further demonstrated that separator pore size plays an essential role in the (002) oriented Zn deposition, resulting in a stable and long cycling performance.

## CRediT authorship contribution statement

**Kesong Yu:** Formal analysis, Investigation, Validation, Visualization, Writing – original draft. **Yuehua Wen:** Formal analysis, Investigation, Validation. **Mengyu Yan:** Conceptualization, Methodology, Supervision, Writing – review & editing. **Xuan Teng:** Formal analysis, Investigation. **Wei Yang:** Visualization. **Sitian Lian:** Formal analysis, Investigation. **Jianyong Zhang:** Validation. **Farao Zhang:** Methodology, Resources. **Xiaoyu Jiang:** Conceptualization, Data curation, Methodology, Writing – review & editing. **Yanzhu Luo:** Methodology, Writing – review & editing. **Liqiang Mai:** Funding acquisition, Supervision.

## Declaration of competing interest

The authors declare that they have no known competing financial interests or personal relationships that could have appeared to influence the work reported in this paper.

## Data availability

Data will be made available on request.

## Acknowledgments

This work was supported by the National Key Research and Development Program of China (2023YFB3809500), the Key Research and Development Program of Hubei Province (2022BAA027), the National Natural Science Foundation of China (22005113), the Science and Technology Industry Fund Project of WUT Technology Transfer Jingmen Center and GEM Co., Ltd. (WHUTJMZX-2022JJ-16, GEM-Q-202302-001), the Wuhan Dawn Plan Project (2023010201020345), the Fundamental Research Funds for the Central Universities (WUT: 2022IVA007, 2022IV015h, 2022IVB008, 2023IVA013; HZAU:2662023PY016), and the self-determined and innovative research funds of Wuhan University of Technology (WUT: 2022-CL-A1-05).

## Appendix A. Supplementary data

Supplementary data to this article can be found online at https://doi.org/10.1016/j.mtener.2023.101488.

## References

[1] H. Pan, Y. Shao, P. Yan, Y. Cheng, K.S. Han, Z. Nie, C. Wang, J. Yang, X. Li, P. Bhattacharya, K.T. Mueller, J. Liu, Reversible aqueous zinc/manganese oxide energy storage from conversion reactions, Nat. Energy 1 (5) (2016) 16039, https://doi.org/10.1038/nenergy.2016.39.

[2] M. Li, Z. Li, X. Wang, J. Meng, X. Liu, B. Wu, C. Han, L. Mai, Comprehensive understanding of the roles of water molecules in aqueous Zn-ion batteries: from electrolytes to electrode materials, Energy Environ. Sci. 14 (7) (2021) 3796–3839, https://doi.org/10.1039/D1EE00030F.

[3] S. Lei, Z. Liu, C. Liu, J. Li, B. Lu, S. Liang, J. Zhou, Opportunities for biocompatible and safe zinc-based batteries, Energy Environ. Sci. 15 (12) (2022) 4911–4927, https://doi.org/10.1039/D2EE02267B.

[4] Z. Liu, Y. Huang, Y. Huang, Q. Yang, X. Li, Z. Huang, C. Zhi, Voltage issue of aqueous rechargeable metal-ion batteries, Chem. Soc. Rev. 49 (1) (2020) 180–232, https://doi.org/10.1039/C9CS00131J.

[5] J. Shin, J.W. Choi, Opportunities and reality of aqueous rechargeable batteries, Adv. Energy Mater. 10 (28) (2020) 2001386, https://doi.org/10.1002/aenm.202001386.

[6] Z. Zhao, R. Wang, C. Peng, W. Chen, T. Wu, B. Hu, W. Weng, Y. Yao, J. Zeng, Z. Chen, P. Liu, Y. Liu, G. Li, J. Guo, H. Lu, Z. Guo, Horizontally arranged zinc platelet electrodeposits modulated by fluorinated covalent organic framework film for high-rate and durable aqueous zinc ion batteries, Nat. Commun. 12 (1) (2021) 6606, https://doi.org/10.1038/s41467-021-26947-9.

[7] R. Guo, X. Liu, F. Xia, Y. Jiang, H. Zhang, M. Huang, C. Niu, J. Wu, Y. Zhao, X. Wang, C. Han, L. Mai, Large-scale integration of a zinc metasilicate interface layer guiding well-regulated Zn deposition, Adv. Mater. 34 (27) (2022) 2202188, https://doi.org/10.1002/adma.202202188.

[8] Y. Dai, C. Zhang, W. Zhang, L. Cui, C. Ye, X. Hong, J. Li, R. Chen, W. Zong, X. Gao, J. Zhu, P. Jiang, Q. An, D.J.L. Brett, I.P. Parkin, G. He, L. Mai, Reversible Zn metal anodes enabled by trace amounts of underpotential deposition initiators, Angew. Chem., Int. Ed. 62 (18) (2023) e202301192, https://doi.org/10.1002/anie.202301192.

[9] F. Wang, O. Borodin, T. Gao, X. Fan, W. Sun, F. Han, A. Faraone, J.A. Dura, K. Xu, C. Wang, Highly reversible zinc metal anode for aqueous batteries, Nat. Mater. 17 (6) (2018) 543–549, https://doi.org/10.1038/s41563-018-0063-z.

[10] L. Cao, D. Li, E. Hu, J. Xu, T. Deng, L. Ma, Y. Wang, X.-Q. Yang, C. Wang, Solvation structure design for aqueous Zn metal batteries, J. Am. Chem. Soc. 142 (51) (2020) 21404–21409, https://doi.org/10.1021/jacs.0c09794.

[11] L. Geng, J. Meng, X. Wang, C. Han, K. Han, Z. Xiao, M. Huang, P. Xu, L. Zhang, L. Zhou, L. Mai, Eutectic electrolyte with unique solvation structure for high-performance zinc-ion batteries, Angew. Chem., Int. Ed. 61 (31) (2022) e202206717, https://doi.org/10.1002/anie.202206717.

[12] B. Yang, Y. Shi, D.J. Kang, Z. Chen, H. Pang, Architectural design and electrochemical performance of MOF-based solid-state electrolytes for high-performance secondary batteries, Interdisciplinary Materials 2 (4) (2023) 475–510, https://doi.org/10.1002/idm2.12108.

[13] Y. Zhang, G. Yang, M.L. Lehmann, C. Wu, L. Zhao, T. Saito, Y. Liang, J. Nanda, Y. Yao, Separator effect on zinc electrodeposition behavior and its implication for zinc battery lifetime, Nano Lett. 21 (24) (2021) 10446–10452, https://doi.org/10.1021/acs.nanolett.1c03792.

[14] C. Wei, L. Tan, Y. Zhang, S. Xiong, J. Feng, Metal-organic frameworks and their derivatives in stable Zn metal anodes for aqueous Zn-ion batteries, ChemPhysMater 1 (4) (2022) 252–263, https://doi.org/10.1016/j.chphma.2021.09.003.

[15] M. Yan, P. He, Y. Chen, S. Wang, Q. Wei, K. Zhao, X. Xu, Q. An, Y. Shuang, Y. Shao, K.T. Mueller, L. Mai, J. Liu, J. Yang, Water-lubricated intercalation in $V_2O_5 \cdot nH_2O$ for high-capacity and high-rate aqueous rechargeable zinc batteries, Adv. Mater. 30 (1) (2018) 1703725, https://doi.org/10.1002/adma.201703725.

[16] C. Xia, J. Guo, Y. Lei, H. Liang, C. Zhao, H.N. Alshareef, Rechargeable aqueous zinc-ion battery based on porous framework zinc pyrovanadate intercalation cathode, Adv. Mater. 30 (5) (2018) 1705580, https://doi.org/10.1002/adma.201705580.

[17] Q. Pang, C. Sun, Y. Yu, K. Zhao, Z. Zhang, P.M. Voyles, G. Chen, Y. Wei, X. Wang, $H_2V_3O_8$ Nanowire/graphene electrodes for aqueous rechargeable zinc ion batteries with high rate capability and large capacity, Adv. Energy Mater. 8 (19) (2018) 1800144, https://doi.org/10.1002/aenm.201800144.

[18] X. Zhang, J. Li, K. Qi, Y. Yang, D. Liu, T. Wang, S. Liang, B. Lu, Y. Zhu, J. Zhou, An ion-sieving janus separator toward planar electrodeposition for deeply rechargeable Zn-metal anodes, Adv. Mater. 34 (38) (2022) 2205175, https://doi.org/10.1002/adma.202205175.

[19] K. Han, F. An, F. Yan, H. Chen, Q. Wan, Y. Liu, P. Li, X. Qu, High-performance aqueous Zn–$MnO_2$ batteries enabled by the coupling engineering of $K^+$ pre-intercalation and oxygen defects, J. Mater. Chem. A 9 (28) (2021) 15637–15647, https://doi.org/10.1039/D1TA03994F.

[20] Y. Lin, Y. Hu, S. Zhang, Z. Xu, T. Feng, H. Zhou, M. Wu, Highly reversible aqueous zinc-ion battery using the chelating agent triethanolamine as an electrolyte additive, CrystEngComm 24 (45) (2022) 7950–7961, https://doi.org/10.1039/D2CE01089E.

[21] G.J. May, A. Davidson, B. Monahov, Lead batteries for utility energy storage: a review, J. Energy Storage 15 (2018) 145–157, https://doi.org/10.1016/j.est.2017.11.008.

[22] J. Liu, Z. Bao, Y. Cui, E.J. Dufek, J.B. Goodenough, P. Khalifah, Q. Li, B.Y. Liaw, P. Liu, A. Manthiram, Y.S. Meng, V.R. Subramanian, M.F. Toney, V.V. Viswanathan, M.S. Whittingham, J. Xiao, W. Xu, J. Yang, X.-Q. Yang, J.-G. Zhang, Pathways for practical high-energy long-cycling lithium metal batteries, Nat. Energy 4 (3) (2019) 180–186, https://doi.org/10.1038/s41560-019-0338-x.

[23] B. Wu, J. Lochala, T. Taverne, J. Xiao, The interplay between solid electrolyte interface (SEI) and dendritic lithium growth, Nano Energy 40 (2017) 34–41, https://doi.org/10.1016/j.nanoen.2017.08.005.

[24] Q. Yang, G. Liang, Y. Guo, Z. Liu, B. Yan, D. Wang, Z. Huang, X. Li, J. Fan, C. Zhi, Do zinc dendrites exist in neutral zinc batteries: a developed electrohealing strategy to in situ rescue in-service batteries, Adv. Mater. 31 (43) (2019) e1903778, https://doi.org/10.1002/adma.201903778.
[25] Z. Wang, J. Huang, Z. Guo, X. Dong, Y. Liu, Y. Wang, Y. Xia, A metal-organic framework host for highly reversible dendrite-free zinc metal anodes, Joule 3 (5) (2019) 1289–1300, https://doi.org/10.1016/j.joule.2019.02.012.
[26] S. Luiso, P. Fedkiw, Lithium-ion battery separators: recent developments and state of art, Curr. Opin. Electrochem. 20 (2020) 99–107, https://doi.org/10.1016/j.coelec.2020.05.011.
[27] L. Sheng, R. Xu, H. Zhang, Y. Bai, S. Song, G. Liu, T. Wang, X. Huang, J. He, The morphology of polyethylene (PE) separator for lithium-ion battery tuned by the extracting process, J. Electroanal. Chem. 873 (2020) 114391, https://doi.org/10.1016/j.jelechem.2020.114391.
[28] W. Zhai, H. Yu, H. Chen, L. Li, D. Li, Y. Zhang, T. He, Stable fouling resistance of polyethylene (PE) separator membrane via oxygen plasma plus zwitterion grafting, Sep. Purif. Technol. 293 (2022) 121091, https://doi.org/10.1016/j.seppur.2022.121091.
[29] Z. Wang, X. Li, N. Dong, B. Liu, G. Tian, S. Qi, D. Wu, Novel $ZrO_2$@Polyimde nano-microspheres-coated polyethylene separators for high energy density and high safety Li-ion battery, Mater, Today Energy 30 (2022) 101155, https://doi.org/10.1016/j.mtener.2022.101155.
[30] Y. Luo, Y. Yang, Y. Tao, D. Huang, B. Huang, H. Chen, Directing the preferred crystal orientation by a cellulose acetate/graphene oxide composite separator for dendrite-free Zn-metal anodes, ACS Appl. Energy Mater. 4 (12) (2021) 14599–14607, https://doi.org/10.1021/acsaem.1c03223.
[31] S.Y. Jin, J. Manuel, X. Zhao, W.H. Park, J.-H. Ahn, Surface-modified polyethylene separator via oxygen plasma treatment for lithium ion battery, J. Ind. Eng. Chem. 45 (2017) 15–21, https://doi.org/10.1016/j.jiec.2016.08.021.
[32] X. Chen, L. Liu, P.Y. Yu, S.S. Mao, Increasing solar absorption for photocatalysis with black hydrogenated titanium dioxide nanocrystals, Science 331 (6018) (2011) 746–750, https://doi.org/10.1126/science.1200448.
[33] G. Wang, H. Wang, Y. Ling, Y. Tang, X. Yang, R.C. Fitzmorris, C. Wang, J.Z. Zhang, Y. Li, Hydrogen-treated $TiO_2$ nanowire arrays for photoelectrochemical water splitting, Nano Lett. 11 (7) (2011) 3026–3033, https://doi.org/10.1021/nl201766h.
[34] B.C. Tripathy, S.C. Das, G.T. Hefter, P. Singh, Zinc electrowinning from acidic sulfate solutions: Part I: effects of sodium lauryl sulfate, J. Appl. Electrochem. 27 (6) (1997) 673–678, https://doi.org/10.1023/A:1018431619595.
[35] Z. Zhao, J. Zhao, Z. Hu, J. Li, J. Li, Y. Zhang, C. Wang, G. Cui, Long-life and deeply rechargeable aqueous Zn anodes enabled by a multifunctional brightener-inspired interphase, Energy Environ. Sci. 12 (6) (2019) 1938–1949, https://doi.org/10.1039/C9EE00596J.
[36] D. Kashchiev, On the relation between nucleation work, nucleus size, and nucleation rate, J. Chem. Phys. 76 (10) (1982) 5098–5102, https://doi.org/10.1063/1.442808.
[37] A. Pei, G. Zheng, F. Shi, Y. Li, Y. Cui, Nanoscale nucleation and growth of electrodeposited lithium metal, Nano Lett. 17 (2) (2017) 1132–1139, https://doi.org/10.1021/acs.nanolett.6b04755.
[38] J. Cao, D. Zhang, Y. Yue, R. Chanajaree, S. Wang, J. Han, X. Zhang, J. Qin, Y. Huang, Regulating solvation structure to stabilize zinc anode by fastening the free water molecules with an inorganic colloidal electrolyte, Nano Energy 93 (2022) 106839, https://doi.org/10.1016/j.nanoen.2021.106839.
[39] T. Wu, C. Ji, H. Mi, F. Guo, G. Guo, B. Zhang, M. Wu, Construction of zwitterionic osmolyte-based hydrogel electrolytes towards stable zinc anode for durable aqueous zinc ion storage and integrated electronics, J. Mater. Chem. A 10 (48) (2022) 25701–25713, https://doi.org/10.1039/D2TA07410A.
[40] Y. Liu, S. Liu, X. Xie, Z. Li, P. Wang, B. Lu, S. Liang, Y. Tang, J. Zhou, A functionalized separator enables dendrite-free Zn anode via metal-polydopamine coordination chemistry, InfoMat 5 (3) (2023) e12374, https://doi.org/10.1002/inf2.12374.
[41] G.D. Wilcox, P.J. Mitchell, Electrolyte additives for zinc-anoded secondary cells I. Brighteners, levellers and complexants, J. Power Sources 28 (4) (1989) 345–359, https://doi.org/10.1016/0378-7753(89)80064-3.
[42] C.J. Lan, C.Y. Lee, T.S. Chin, Tetra-alkyl ammonium hydroxides as inhibitors of Zn dendrite in Zn-based secondary batteries, Electrochim. Acta 52 (17) (2007) 5407–5416, https://doi.org/10.1016/j.electacta.2007.02.063.
[43] J.-L. Yang, J. Li, J.-W. Zhao, K. Liu, P. Yang, H.J. Fan, Stable zinc anodes enabled by a zincophilic polyanionic hydrogel layer, Adv. Mater. 34 (27) (2022) 2202382, https://doi.org/10.1002/adma.202202382.
[44] G. Trejo, H. Ruiz, R.O. Borges, Y. Meas, Influence of polyethoxylated additives on zinc electrodeposition from acidic solutions, J. Appl. Electrochem. 31 (6) (2001) 685–692, https://doi.org/10.1023/A:1017580025961.
[45] J.C. Ballesteros, P. Díaz-Arista, Y. Meas, R. Ortega, G. Trejo, Zinc electrodeposition in the presence of polyethylene glycol 20000, Electrochim. Acta 52 (11) (2007) 3686–3696, https://doi.org/10.1016/j.electacta.2006.10.042.
[46] L. Miao, R. Wang, W. Xin, L. Zhang, Y. Geng, H. Peng, Z. Yan, D. Jiang, Z. Qian, Z. Zhu, Three-functional ether-based co-solvents for suppressing water-induced parasitic reactions in aqueous Zn-ion batteries, Energy Storage Mater. 49 (2022) 445–453, https://doi.org/10.1016/j.ensm.2022.04.032.
[47] A. Chen, C. Zhao, Z. Guo, X. Lu, N. Liu, Y. Zhang, L. Fan, N. Zhang, Fast-growing multifunctional $ZnMoO_4$ protection layer enable dendrite-free and hydrogen-suppressed Zn anode, Energy Storage Mater. 44 (2022) 353–359, https://doi.org/10.1016/j.ensm.2021.10.016.
[48] D.S. Ullah, A. Badshah, F. Ahmed, R. Raza, A. Altaf, R. Hussain, Electrodeposited zinc electrodes for high current Zn/AgO bipolar batteries, Int. J. Electrochem. Sci. 6 (2011), https://doi.org/10.1016/S1452-3981(23)18290-3.
[49] T. Wang, J. Sun, Y. Hua, B.N.V. Krishna, Q. Xi, W. Ai, J.S. Yu, Planar and dendrite-free zinc deposition enabled by exposed crystal plane optimization of zinc anode, Energy Storage Mater. 53 (2022) 273–304, https://doi.org/10.1016/j.ensm.2022.08.046.
[50] J.Y. Chen, M.J. Zhu, M.T. Gan, X.L. Wang, C.D. Gu, J.P. Tu, Rapid electrodeposition and corrosion behavior of Zn coating from a designed deep eutectic solvent, Metals 13 (1) (2023), https://doi.org/10.3390/met13010172.